New Journal of Physics
The open access journal at the forefront of physics

Deutsche Physikalische Gesellschaft DPG
IOP Institute of Physics

Published in partnership with: Deutsche Physikalische Gesellschaft and the Institute of Physics

OPEN ACCESS

RECEIVED
30 September 2020

REVISED
25 January 2021

ACCEPTED FOR PUBLICATION
8 February 2021

PUBLISHED
15 March 2021

PAPER

Generation of ultrashort keV Ar^+ ion pulses via femtosecond laser photoionization

Alexander Golombek*, **Lars Breuer**, **Lisa Danzig**, **Paul Kucharczyk**, **Marika Schleberger**, **Klaus Sokolowski-Tinten** and **Andreas Wucher**

Universität Duisburg-Essen, Fachbereich Physik, Lotharstraße 1, 47057 Duisburg, Germany
* Author to whom any correspondence should be addressed.

E-mail: alexander.golombek@uni-due.de and andreas.wucher@uni-due.de

Keywords: ion solid interaction, ultrashort ion pulses, femtosecond laser ionization, strong field photoionization, tunnel ionization, ion bunching

Abstract

Ion beams with energies in the keV regime are widely utilized in solid-state physics, but the ultrafast dynamics triggered by an ion impact onto a solid surface is to date exclusively accessible via simulations based on many untested assumptions and model parameters. A possible experimental access rests on the availability of a laser-synchronized ion source delivering sufficiently short ion pulses for time resolved pump–probe experiments. Here, we demonstrate a new miniaturized ion optical bunching setup for the creation of rare gas ion pulses using strong-field femtosecond laser photoionization. Neutral Ar gas atoms at room temperature are intercepted by a 50 fs, 800 nm laser pulse focused to $\sim$10 μm spot size. We demonstrate the generation of monoenergetic 2 keV Ar^+ ion pulses with 180 ps duration (FWHM) at laser peak intensities around 10^{14} W cm^{-2} and of multiply charged Ar^{q+} ions ($q = 1$–5) at higher laser intensities. The results are in good agreement with detailed ion trajectory simulations, which show that the temporal resolution is essentially limited by the initial (thermal) velocity spread of the generated photo-ions, indicating the possibility to achieve even better time resolution by cooling the gas prior to ionization.

1. Introduction

Ion beams are used in many scientific and technological applications and indispensable especially in the context of nanotechnology, since their potential for manipulating and analyzing matter on the atomic scale is unprecedented [1–3]. Apart from their routine use in surface analysis, they have been used to achieve superplastic nanoscale pore shaping [4], to image the nanophotonic modes of microresonators [5], to perform isotopic nanoscopy [6], to analyze the solid-electrolyte interphase of lithium-ion batteries [7], and almost regularly to fabricate nitrogen vacancy centers in diamonds to be used as qubits [8–11], to name just a few recent examples. In addition, ion beams particularly in the kiloelectronvolt impact energy range are being routinely used for the production, structuring and characterization of nanoscale surface coatings and devices [12]. However, this widespread and self-evident use lets us overlook that from experiments we know next to nothing about the initial non-equilibrium state induced by an ion impact as well as the subsequent dynamics. This serious lack of knowledge is inherently connected to the lack of ultrashort ion pulses, which could be used in state-of-the-art pump–probe experiments in order to study the ion-induced dynamics in real time. In contrast to lasers, where pulses well below 100 attoseconds can now be generated [13, 14], the development of short keV ion pulse sources stopped just below 1 ns [15].

When an energetic ion or atom impinges onto a solid surface, various particles such as secondary ions, neutrals, electrons or photons can be excited and emitted due to the transfer of kinetic or potential energy from the projectile to the solid. Moreover, the projectile can be backscattered from the bombarded solid in various excitation or charge states. Computer simulations suggest that the microscopic energy transfer processes underlying the backscattering or emission of particles [16–18] as well as the related charge

transfer and excitation dynamics [19–23] occur on extremely fast time scales on the order of picoseconds or below. Measured data on, for instance, the neutralization efficiency of projectile ions penetrating thin targets, the characteristics of backscattered projectiles as well as emitted surface particles, electrons or photons provide experimental evidence supporting this notion. In practically all experiments, however, asymptotic stages at the end of the ion-induced energy transfer processes are detected, while the underlying microscopic non equilibrium dynamics must be inferred from comparison with theoretical model calculations [24]. In order to overcome this limitation and gain a more direct experimental insight into the ion-induced dynamics, we therefore currently pursue the strategy to establish a pump–probe technique using a laser-synchronized ultrashort ion pulse as a stimulus (pump) in connection with a laser-based analysis technique (probe) to follow, for instance, the ion-induced local order–disorder transition, transient electronic excitation or particle emission in a time resolved manner.

As a necessary prerequisite for such an endeavor, it is essential to develop concepts for the production of ultrashort ion pulses at ion energies in the keV regime. In state-of-the-art ion sources used, for instance, in high resolution TOF instruments, ion packages of several nanoseconds length are generated via chopping of a continuous ion beam and then compressed in time by bunching in a time dependent electric field located somewhere downstream the beam line. Using this technique, it is now routinely possible to generate nanosecond or even sub-nanosecond pulses of ions like Ga^+, $Bi_{(n)}{}^+$ or $Au_{(n)}{}^+$ [25] at ion energies of the order of several ten keV. Using a similar concept, Linnarsson *et al* have demonstrated the generation of 100 keV proton pulses with a duration of about 400 ps for use in high resolution medium energy ion scattering experiments [26]. In order to arrive at the (sub-)picosecond time regime necessary for direct time resolved studies of the ultrafast ion-induced dynamics, we have recently developed a concept to generate quasi-monoenergetic rare gas ion pulses at ion energies in the few keV range, which are synchronized with a femtosecond laser pulse to allow for an optically delayed pump–probe experiment [27]. The basic idea is to generate the ions via photoionization by intersecting a cloud of rare gas atoms with a tightly focused laser beam. The ions generated this way are then accelerated in the direction perpendicular to the laser propagation within an ion-optical bunching setup providing flight time focusing at the target surface. Due to the small extension of the effective ionization volume within the laser focus, the energy spread introduced by different starting positions of the ions within the (static) buncher field remains negligible. In order to allow a manageable optical delay between pump and probe pulses, the total ion flight time must not exceed a few 10 ns. As a consequence, the entire buncher needs to be strongly miniaturized to ensure an ion flight path of only a few mm length. In this work, we therefore test the combination of a tightly focused femtosecond laser beam with such a miniaturized buncher setup via photoionization of neutral Argon gas atoms backfilled into the ionization chamber at room temperature and detection of the resulting Ar^{q+} ions by a fast multichannel plate (MCP) detector mimicking the target surface. The aim is to gain a fundamental understanding of the buncher regarding its exact geometry, its flight time focusing properties, the role of different boundary conditions as well as photoionization properties like the mean number of ions created per laser pulse and the charge state distribution of the generated ions. We will show that it is possible to generate a 2 keV Ar^+ ion pulse with a duration of the order of 100 ps at a total ion flight time well below 100 ns. This result will be compared to detailed numerical ion trajectory simulations, which show that the achieved pulse width is essentially determined by the thermal velocity spread of the generated photo-ions, thereby opening the possibility to further improve the temporal resolution via cooling of the neutral precursor gas.

2. Methods

The experimental setup consists of an ultrahigh vacuum (UHV) chamber, which contains the ion buncher as well as the MCP detector, and a tabletop laser system to produce femtosecond laser pulses passing the vacuum chamber as described in detail below. A schematic of the experimental setup within and outside the UHV chamber (blue box) as well as a blow-up of the actual ion buncher is depicted in figure 1.

The tabletop laser system produces laser pulses of ∼50 fs duration at a repetition rate of 1 kHz and a wavelength of 800 nm. A beam splitter reflects about 1% of the laser radiation onto a fast avalanche photodiode (BPW-28), which provides a starting trigger signal for the ion flight time measurement (see below). The combination of a $\lambda/2$ plate with a polarizing filter in the beamline allows to adjust the intensity of the laser beam, with the maximum average output power being measured with a power meter (Coherent FieldMate) as 1.4 W before the last mirror. The circularly shaped laser beam is subsequently focused by an off-axis parabolic mirror ($f = 101.6$ mm) to a 10 μm (FWHM) waist diameter into the gap between the electrodes E_1 and E_2 with a lateral diameter of 11 mm each, where the focusing element is translatable on a micrometer *xyz* stage to precisely steer the laser focus position above an 80 μm diameter pinhole in the center of E_2 (see inset of figure 1). In the focal plane, the laser yields a maximum achievable peak power

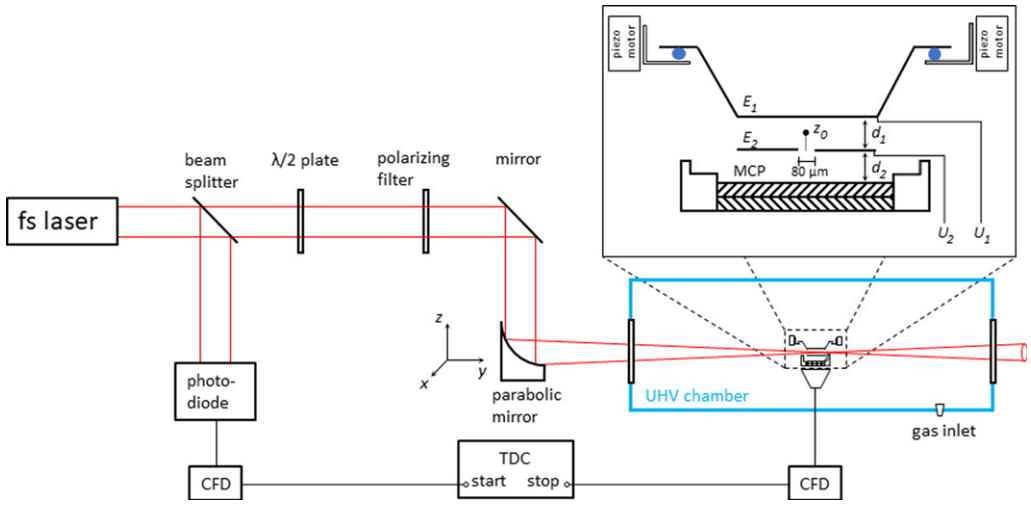

Figure 1. Schematic of the experimental setup. The femtosecond laser beam is focused into the UHV ionization chamber (blue box) via an off-axis parabolic mirror mounted on a *xyz* manipulator. A fast photodiode monitors the firing of the laser pulse to a start input for a TDC, the stop input is given by ions hitting the MCP detector. Piezo motors allow to move the upper electrode $E1$ against the stack of $E2$ and detector to ensure a parallel electric field and a defined distance $d1$ (see inset). Argon gas can be backfilled into the UHV chamber via a gas inlet.

density of about 3.5×10^{16} W cm^{-2}. The third (target) electrode E_3 of the buncher setup is formed by the front of an ultrafast MCP detector (Photonis Gen2 TOF Detector) below E_2, which is optimized to provide an ultimate time resolution on the order of 50 ps (manufacturer specification). The distance d_2 between E_2 and the MCP front is fixed to a few mm by a machined ceramic (MACOR) insulator, while the distance d_1 as well as the angular tilt between E_1 and E_2 can be adjusted with sub-micron precision using three piezo motors (SmarAct SLC-1720) connected to the upper electrode via isolating sapphire balls. The three-electrode bunching setup represents a so-called Wiley-McLaren configuration [28], which allows to adjust the two electric fields in order to ensure first order flight time focusing for ions starting in an *xy*-plane located at any position z_0 along the ion extraction direction z. For that purpose, each electrode can independently be set to a selectable electric potential between zero and ± 10 kV with respect to ground. In the setup used for the present work, the collector electrode of the MCP detector was grounded, and the potential at the MCP front was set to $U_{\mathrm{MCP}} = -2000$ V to provide sufficient gain to efficiently detect single ion pulses. The potential at E_2 was chosen as $U_2 = -2000$ V as well, resulting in a zero electric field between E_2 and E_3. For symmetry reasons, the potential at the upper electrode E_1 was set to $U_1 = +2000$ V. Under these conditions, first order flight time focusing occurs for ions starting at a position

$$z_0 = d_2/2 \tag{1.1}$$

above the upper surface of electrode E_2, and the total ion flight time to electrode E_3 is given by

$$t = \sqrt{\frac{m\, d_1}{qe\, \Delta U}} \times \left(\sqrt{2\, z_0} + \frac{d_2}{\sqrt{2\, z_0}} \right), \tag{1.2}$$

with m being the mass of a given ion and q its charge state, e denoting the elementary charge and ΔU the total potential difference between E_1 and E_2.

Since the laser focus of 10 μm diameter needs to be positioned and centered above the 80 μm aperture in electrode E_2, a coarse alignment was performed under atmospheric conditions by removing the top electrode and positioning the focal spot above the center of the second electrode by eye. In doing so, we make use of a clearly visible local electrical breakdown in air around the laser focus. In addition, the laser beam profile was monitored at the exit window of the UHV chamber and adjusted to a rotationally symmetric shape via self-modulation of the beam, which is a good indicator of a well-aligned beam line with the parabolic mirror. After repositioning the top electrode, the vacuum chamber was pumped down to a base pressure of 3×10^{-8} mbar using a 300 l s^{-1} turbomolecular pump. During the ionization experiment, the chamber was homogeneously back-filled with Argon gas with a partial pressure of 7×10^{-7} mbar (pressure reading of 9×10^{-7} mbar from a calibrated ion gauge (Leybold IoniVac ITR 90) corrected by a factor 0.8 for Argon as specified by the manufacturer). After applying the specified voltages, the laser intensity was set to an average power of about 16 mW measured with a laser power meter

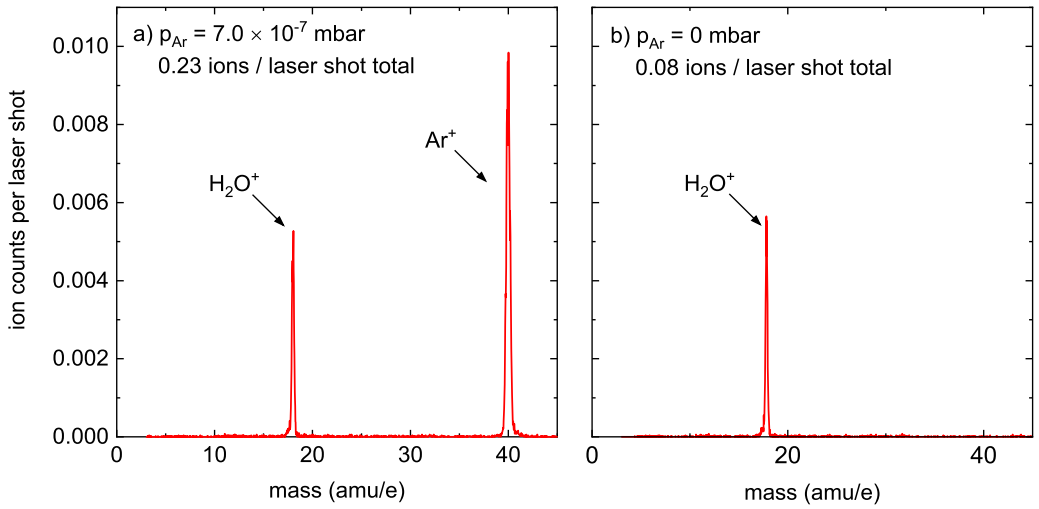

Figure 2. Comparison of first TOF mass spectra obtained with (a) Argon gas back-filled into the ionization chamber and (b) the residual gas only with a laser peak power density of 4.3 × 10^{14} W cm^{-2} at 800 nm.

(Coherent FieldMate) in the beam before the parabolic mirror, which is subsequently focused to a peak power density of about 4.3 × 10^{14} W cm^{-2}. For the production of Ar^+ ions (IP = 15.76 eV), this leads to a Keldysh parameter of $\gamma = \sqrt{\mathrm{IP}/2U_\mathrm{p}} = 0.55$ (with U_p being the ponderomotive potential of an electron in the 800 nm laser field), thereby indicating a tunnel ionization process [29].

Subsequently, ions created at the laser focus located between E_1 and E_2 were accelerated along the z-direction (perpendicular to the laser beam) towards the MCP detector, thereby passing through the aperture in E_2. A single ion hitting the detector produced an output pulse with an average height of about 30 mV at the 50 Ω termination of the collector, which was then processed using a specially selected fast preamplifier in combination with a constant fraction discriminator (CFD) (both manufactured by Surface Concept GmbH, Mainz, Germany) delivering a time resolution below 50 ps as specified by the manufacturer. A properly matched time-to-digital converter (TDC) (Surface Concept-TDC-1000/02 D) triggered by the photodiode signal then recorded the arrival time of the incoming ions relative to the firing of the laser with a bin width of 27.4 ps. For that purpose, the output pulses of the photodiode were processed by another CFD (Ortec Model 935 Quad 200 MHz CFD), thereby ensuring a time jitter of the starting pulse of typically 25 ps. The laser intensity was adjusted such that less than a single ion of the desired charge state was produced per laser pulse, and the kHz repetition of this experiment then allows to sum over all detected ions, thereby generating a flight time spectrum which corresponds to the arrival time distribution of the ions at the target surface (here: the MCP detector). The total flight time determined by the peak in the measured TOF distribution then allows to clearly separate between different ion species and/or charge states.

The first TOF spectrum measured under these conditions is shown in figure 2(a). The two detected peaks are identified as arising from H_2O^+ and Ar^+ ions, respectively. The corresponding blank spectrum measured without Argon gas inlet is shown in figure 2(b). It is seen that the Ar^+ peak is completely absent in the blank spectrum, while the H_2O^+ peak remains unchanged and must therefore clearly originate from residual gas ionization. Comparing the total number of counts detected in both spectra, we find that an average of 0.15 Ar^+ and 0.08 H_2O^+ ions are generated per single laser shot. At first glance, this ratio appears surprising in view of the much larger ratio (>20) between the number density of back-filled Ar atoms and residual gas H_2O molecules, respectively. We attribute this finding to the fact that the ionization potential of H_2O molecules (12.6 eV) is significantly lower than that of Ar atoms, thus making the strong-field photoionization process more efficient for water. As a consequence, the effective ionization volume for H_2O^+ formation is much larger than that for Ar^+ formation. As a side remark, we mention that a TOF spectrum similar to that depicted in figure 2(a) has been reported by Höhr *et al* [15] using a similar concept to generate sub-nanosecond Ar^+ ion pulses as employed here.

It should be noted, however, that the H_2O^+ ion peak was found to decrease in intensity with time after pumpdown of the chamber. In fact, the observed decrease was more pronounced than that of the measured residual gas pressure, indicating that outgassing of the buncher electrodes led to a higher water partial pressure within the buncher electrode gap. After sufficient pumping time, the water peak therefore practically disappeared from the measured spectra.

3. Results and discussion

3.1. Lateral laser scan

After the successful detection of laser-ionized Argon ions, a first measurement was performed by scanning the laser focus along the x-axis, i.e. in a direction parallel to the electrode surfaces but perpendicular to the laser beam propagation. The result is depicted in figure 3, where the integrated total number of detected Ar^+ ions is plotted against the x-position of the focusing parabolic mirror.

In acquiring the data, spectra were summed for a burst of 1000 laser shots and then averaged over a total number of 20 such bursts. In interpreting the data of figure 3, it is of note that the signal measured at a specific x-position represents an integral of the photoionization efficiency $p_i(x, y)$ convoluted with the ion-optical transmission function $T(x, y)$. While the former is connected with the spatial laser intensity distribution $I_L(x, y)$ in directions perpendicular and parallel to the laser beam, the latter is determined by the diameter d of the aperture in electrode E_2 and should be roughly given as

$$T(x,y) = \begin{cases} 1 & \text{for } x^2 + y^2 \leqslant d^2/4 \\ 0 & \text{elsewhere} \end{cases} .$$

Due to the strongly non-linear laser intensity dependence of p_i, it is not easy to predict the expected behavior. The indicated curve included in figure 3 corresponds to a least square fit of an arbitrarily selected Gaussian function which yields a FWHM of 30 μm. Detectable signal is observed in a range of $6\sigma_x \approx 2.55 \times \text{FWHM} = 76.5 \pm 4$ μm, which roughly corresponds to the 80 μm diameter aperture in electrode E_2. The fit indicates the distribution to be centered at $x = 8.115$ mm, which is therefore identified as the position of the ion optical axis through the center of that aperture. For the remainder of this work, the laser x-position was set to and kept at this value.

Apart from the laser alignment, there is another important conclusion that can be drawn from the data plotted in figure 3. In our previous work using a VUV laser beam in order to characterize a supersonic Argon expansion, we found that the laser induced Ar^+ ion signal was actually generated by electron impact ionization via photoelectrons produced somewhere in the ionization chamber. Back then, the characteristic signature of this 'photoelectron-impact ionization' process was the observation that the measured ion signal was essentially independent of the laser beam focus position. In pronounced contrast, here we detect no ion signal at all if the laser focus is positioned outside the ion-optical acceptance window of the buncher electrodes, thereby clearly demonstrating that the detected ions are indeed produced via photoionization. This finding is important in view of the targeted application, since it shows that the influence of secondary electrons produced by laser stray light hitting the electrode in our strongly miniaturized buncher setup is negligible.

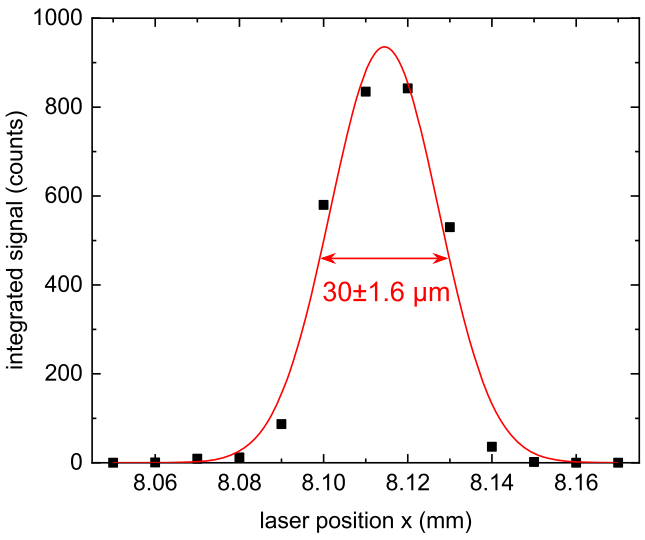

Figure 3. Scan of the laser position along the x direction above the 80 μm aperture in electrode $E2$. The total integrated signal measured at each laser position is displayed per burst of 1000 laser pulses. Solid line: least square fit of Gaussian function to the data in order to extract the indicated FWHM of the distribution.

3.2. Flight time focusing

In order to determine the optimum flight time focusing position z_0 along the ion extraction axis z perpendicular to all electrodes, flight time distributions of the generated photoions were measured as a function of the laser focus position. Figure 4 displays the resulting measurement for Ar^+ ions generated at a moderate laser peak intensity of about 10^{14} W cm^{-2}. For comparison, the theoretically expected behavior according to equation (1.2) was fitted to the data as shown by the solid line.

It is seen that the theoretical expectation describes the measured data quite well, so that the fit allows to extract the exact values of the geometrical distances $d_1 = (2.6 \pm 0.12)$ mm and $d_2 = (2.92 \pm 0.035)$ mm, respectively, as well as the flight time focus position $z_0 = 1.45$ mm, i.e. at $d_2/2$ above electrode E_2 in accordance with equation (1.1). Once the exact geometry is known, we can compare the measured ion arrival time with the total ion flight time of about 54 ns calculated for 2 keV Ar^+ ions from equation (1.2) using $\Delta U = 4$ kV. As a result, it is found that an offset of $t_0 = (11.7 \pm 1.7)$ ns needs to be subtracted from the measured arrival time in order to match the flight time, which likely results from the difference in cable lengths and processing times of the electronics connected to the photodiode monitoring the laser pulse and the ion detector, respectively.

As a next step, we evaluate the width of the Ar^+ arrival time distribution by arbitrarily fitting a Gaussian function to the measured TOF peak. This method is chosen rather than directly measuring the FWHM of the binned flight time distribution, since (i) it is not easy to exactly identify the peak maximum from the binned data and (ii) the fitting procedure reduces the error introduced by statistical noise. The resulting FWHM is plotted against the ion starting coordinate in figure 5, where a plateau of 200 to 220 ps is visible between $z = 1.1$ and 2.3 mm. The rise at the left and right side likely results from blocking the laser due to geometric constraints, thus distorting the pulse shape and the FWHM of the arrival time distribution. Since the ionizing laser pulse is very short (∼50 fs) and space charge broadening is absent for the single ion pulses recorded here, the observed width is determined by the statistical distribution of ion starting positions and initial velocities. The flight time dispersion induced by the spread of starting positions can be visualized from the slope of the curve displayed in figure 4. The resulting 'geometric' dispersion obviously depends on the laser position. Its magnitude can easily be estimated by convoluting the Gaussian laser intensity profile with the curve plotted in figure 4. In fact, this will overestimate the geometric dispersion, since the ionization probability depends on the laser intensity in a strongly nonlinear manner, so that the real ionization profile will be narrower than the laser intensity profile. A more realistic estimate of this effect is described in references [27, 30] and used in the numerical simulations described below in section 3.4. In any case, it is evident from figure 5 that geometric broadening is minimized if the laser is positioned at or close to the flight time focusing position $z_0 = 1.45$ mm determined by the local minimum in figure 4. Interestingly, the smallest pulse width is not observed at exactly this position, but rather at $z_{opt} = 1.85$ mm, i.e. 0.4 mm farther away from electrode E_2. Estimating the remaining geometric dispersion at z_0 and z_{opt}, one arrives at a geometric flight time broadening of a few picoseconds, which is much smaller than the actually observed width of about 200 ps (see further below), indicating that the pulse width cannot be significantly influenced by the buncher's flight time focusing properties in this regime.

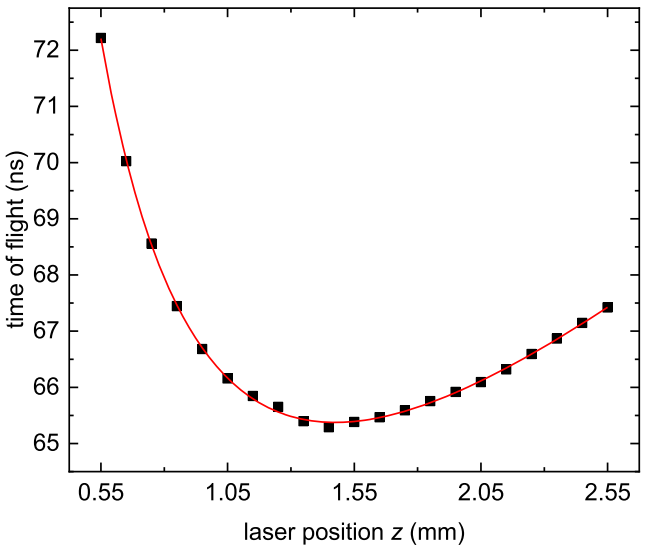

Figure 4. Measured time of flight as a function of the laser position z. Solid line: least square fit of the expected theoretical behavior according to equation (1.2) using the values of d_1 and d_2 and a flight time offset t_0 as fit parameters (see text).

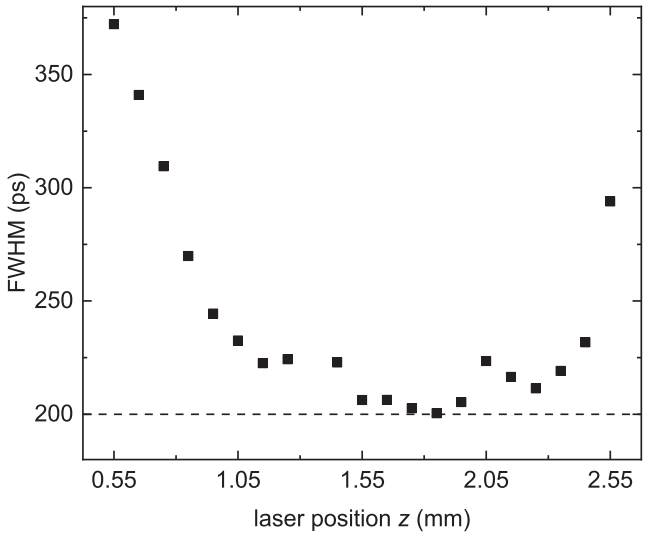

Figure 5. Temporal widths (FWHM) of the measured Ar^+ TOF distributions vs the ionization laser focus position z. The distributions were accumulated from around 1.8×10^4 single ion impacts generated in 2×10^4 laser shots.

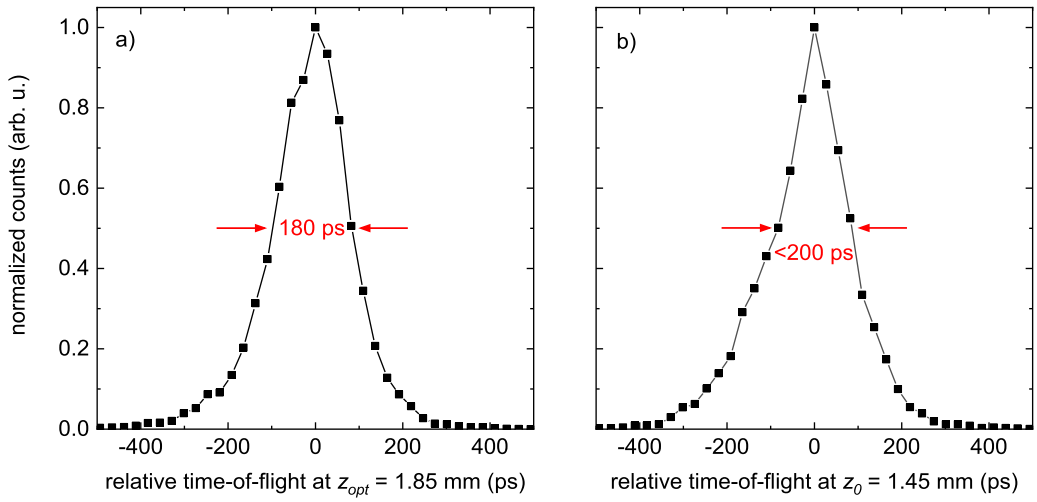

Figure 6. Arrival time distribution of 2 keV Ar^+ ions measured with the photoionization laser focus positioned at $z_{opt} = 1.85$ mm (a) and $z_0 = 1.45$ mm (b). The ions were registered at the front electrode of a fast MCP detector mimicking the target surface E_3 of the three-electrode ion buncher. For the definition of z_{opt} and z_0 see text.

The second critical effect influencing the measured pulse width is the distribution of the starting velocities of the ions at the beginning of their acceleration. Since the experiments reported here were performed with Argon gas introduced at room temperature, the corresponding velocity distribution is determined by the thermal motion of the neutral Ar atoms, which remains essentially unchanged upon photoionization and therefore holds for the laser-generated ions as well. In principle, it is relatively easy to estimate the order of magnitude of the flight time dispersion induced by this thermal velocity spread. For that purpose, it is convenient to calculate the turn-around time of an ion starting with initial velocity v_0 in the direction *opposite* to the ion extraction. This ion will then initially be decelerated in the extraction field, until it comes to a stop, turns around and reaches its original z-position again after a time t_z. From that point on, it will follow exactly the same trajectory as another ion initially starting with the same velocity v_0 directed *along* the ion extraction axis. Calculating t_z for an average thermal velocity $\overline{v}_z = \sqrt{2k_B T/\pi m}$ of Ar atoms at room temperature yields a thermal flight time broadening of the order of 100 ps in reasonable agreement with the data in figure 5. A more detailed simulation of the ion flight time distribution including the thermally induced flight time broadening is described in section 3.4 below.

The raw data of the sharpest ion flight time distribution measured with the laser focus positioned at the optimum position $z_{opt} = 1.85$ mm is shown in figure 6(a). The distribution was accumulated over 2×10^4 laser shots with the detection of 0.9 single 2 keV Ar^+ ions per shot, thereby virtually excluding any space

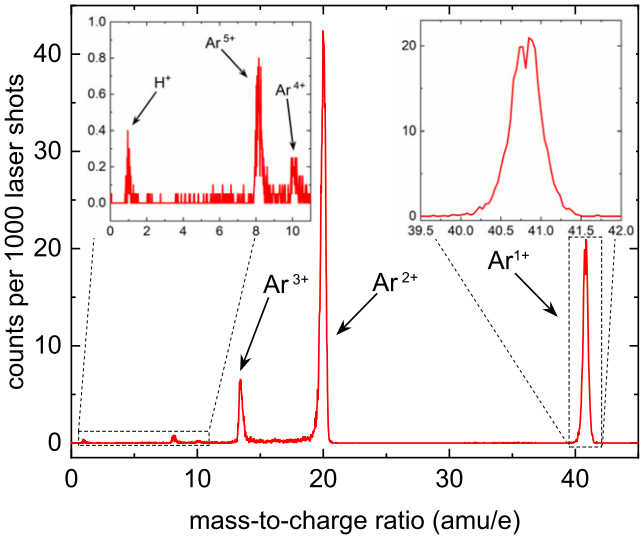

Figure 7. Flight time spectrum measured at the nominal flight time focus position z_0 and with an increased laser peak intensity of 2.4×10^{16} W cm^{-2} under otherwise identical conditions as used before. The bottom axis was converted to apparent m/q values in order to unambiguously identify the signals arising from multiply charged Ar^{q+} ions. Left insert: zoom of small signals detected for $q = 4$ and 5 as well as for H^+. Right insert: zoom of Ar^+ ion signal.

charge broadening. It is seen that the ion arrival time distribution at the MCP detector exhibits a fairly symmetric shape with a width of 180 ps (FWHM). For comparison, figure 6(b) shows similar distribution measured at the nominal flight time focusing position z_0, which is seen to exhibit a slightly more asymmetric shape with, however, nearly the same width as the one measured at z_{opt}. To our knowledge, the data displayed in figure 6 constitute the sharpest time resolution reached to date for the impact of heavy ions with keV energies. The above estimate shows that the pulse width is largely determined by the thermal velocity spread of the neutral gas atoms prior to photoionization. In order to shorten the pulse width further, it is therefore necessary to cool the gas. In fact, it is easy to estimate that a gas temperature of the order of 0.1 K or below would be needed in order to allow the generation of ion arrival time distributions with ∼1 ps width.

3.3. Charge states

A further aspect of the investigated short-pulse ion source is the possibility to generate multiply charged ions as well. In principle, one would expect a sequential appearance of higher charge states with increasing laser intensity, while at the same time lower charge states become sequentially depleted. In order to demonstrate this possibility, the laser peak intensity was increased by about two orders of magnitude and the flight time spectrum was measured at the nominal flight time focus position z_0 under otherwise identical conditions as applied before. The resulting data are displayed in figure 7. In order to unambiguously identify the peaks of multiply charged ions in the measured spectrum, the bottom axis was converted from flight time to apparent mass-to-charge ratio.

At the particular laser intensity chosen here, one observes a dominant Ar^{2+} ion peak, but Ar^{3+} is already clearly detectable. As shown in the left insert, Ar^{4+} and Ar^{5+} ions are also detected, albeit with relatively low intensity. Integrating the measured peaks, one obtains an Ar^{3+}/Ar^{2+} ratio of about 0.2. It is not easy to compare this value with published literature data, since most of the corresponding experiments—and particularly those performed for Ar^{q+} ions—were performed without restriction of the effective ionization volume (see, for instance reference [31]). Hänsch *et al* [32] have developed a technique to restrict this volume by means of a pinhole in the ion extraction electrode, which is similar to our setup with a 80 μm diameter pinhole in electrode E_2. Under these conditions, the charge state distribution of Xe^{q+} ions was measured as a function of the central laser intensity for a similar laser beam as used here. With increasing intensity, a maximum Xe^+ ion count was found at around 1×10^{14} W cm^{-2}, which then decreases and transforms to an increasing Xe^{2+} signal and a slowly rising count rate of Xe^{3+} as well. In principle, such a behavior is in accordance with standard tunnel ionization theory [33], which predicts sequential maxima of increasing charge states with increasing laser intensity. Although not shown, we note that we observe a similar behavior for our Ar^{q+} signals as well. It is, however, quite remarkable that the Ar^{5+} signal in figure 7 is about 3.5 times higher than that for Ar^{4+}, which is contra-intuitive and provides a clear indication of a non-sequential multiple ionization process.

As expected and discussed above, the signal of singly charged Argon ions can still be seen in figure 7, albeit at reduced intensity compared to doubly charged ions. A blow-up of the respective flight time distribution is shown in the right insert. It is seen that (i) the most probable flight time of the Ar^+ ions is slightly above that expected for $m/q = 40$ and (ii) the flight time distribution exhibits a double-peak structure. We attribute this behavior to the fact that these ions are not created in the center of the laser focus but originate from the wings of the beam profile where the laser intensity is lower. Their starting position is therefore slightly off the flight time focusing position z_0 corresponding to minimum flight time. As a consequence, these ions need longer times to reach the detector and therefore appear at later times in the flight time spectrum, therefore appearing at a higher m/q in the converted mass spectrum. The double peak structure observed for the Ar^{1+} ions supports this interpretation, since the ion flight times on both sides of z_0 show a slightly asymmetric behavior (see figure 4). In summary, the data shown here prove that it is possible to generate short pulses of multiply charged ions with charge states up to at least $q = 5$, thereby enabling the study of charge-state effects on the ion-induced non-equilibrium dynamics.

3.4. Comparison to numerical simulations

To understand and predict the properties of the generated ion pulses, detailed numerical simulations are being performed in our research group. In these simulations, a realistic model is used including both the formation of ions from a thermal ensemble of neutral gas atoms via strong-field laser photoionization and their trajectories in the buncher field. A detailed description of the used procedure can be found in references [27, 30]. Briefly, the buncher electrode geometry is implemented in the charged particle optics code and the electric fields are calculated by numerically solving the Laplace equation. The calculated field configuration is then transmitted to the generalized particle tracker code in order to follow the ion trajectories. As starting conditions, the initial ion positions are randomly chosen according to a probability distribution calculated from the laser profile using standard strong-field photoionization theory [33]. Their starting velocity is then randomly chosen according to thermal distributions for the three velocity components (v_x, v_y, v_z) using, e.g. different temperature values for each direction. Depending on the laser intensity, clouds of ions with different charge states are generated this way, the trajectories of which are then traced by explicitly taking into account the space charge interaction between all individual ions at each time step. In view of the experiments performed here, we calculated the flight time distribution for ions starting with an isotropic thermal velocity distribution at room temperature. Figure 8(a) shows the resulting simulated arrival time distribution of single Ar^+ ions starting at a temperature of 300 K. For comparison, figure 8(b) shows the flight time distribution calculated for the same ions starting at a temperature of 0 K.

It is obvious that the shape of the simulated room temperature distribution is entirely dominated by the thermal ion starting velocity spread, rendering the influence of geometric flight time dispersion as seen in figure 8(b) negligible. Probably the most important observation is that the predicted distribution in figure 8(a) closely resembles the experimentally measured distributions displayed in figure 6. In particular, the simulated pulse width of 150 ps is in astonishingly good agreement with the measured width of 180 ps in figure 6(a). Furthermore, the pulse shapes are comparable as well, both resembling a Gaussian profile

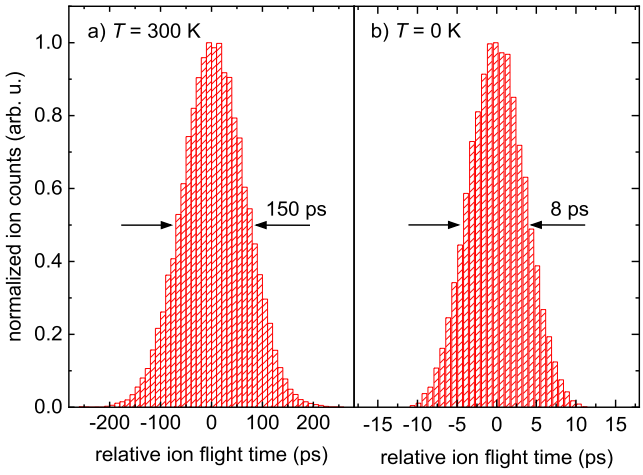

Figure 8. Simulated flight time histogram of singly charged Ar^+ ions calculated for the same buncher geometry as used in the experiments. The starting positions of the ions were randomly selected according to a calculated photo-ionization efficiency profile, while the starting velocities were randomly selected according to a thermal distribution at a temperature of 300 K (a) and 0 K (b), respectively.

with nearly symmetric sides. The remaining difference between predicted and measured pulse widths likely results from various possible experimental errors, such as not perfectly aligned electrodes, the limited time resolution of the MCP detector as well as potential time jitter of the TDC starting pulse. Nevertheless, the fact that comparable pulse shapes are observed in experiment and simulation provides a good indication for the functionality of the ion buncher setup on one hand and lends credibility to the simulation procedure on the other hand, especially in hindsight of our planned future experiments with ultracold atoms. We are confident that the ion flight time distribution of 8 ps pulse width simulated for $T = 0$ K, as shown in figure 8(b), can be further compressed to (sub-)picosecond range by properly adjusting the electric field strengths for an optimal flight time focus within the buncher setup.

4. Conclusion and outlook

The data presented here demonstrate that it is possible to generate short Argon ion pulses with sub-nanosecond (<200 ps) duration at an ion energy of only 2 keV. The results obtained here also show that the investigated ion source allows the generation of short, multiply charged Ar^{q+} ion pulses as well. More specifically, we demonstrate that with the given laser system we are able to control the charge state of the created ions at least up to $q = 5$.

To our knowledge, the measured pulse width of 180 ps represents the best time resolution of a keV ion pulse that has been reported so far. This result is exciting, since the ions are being generated via photoionization, so that the generated ion pulses are inherently synchronized with a femtosecond laser pulse. Consequently, the pulses can be utilized in a pump–probe experiment, where the probe is triggered by the same, optically delayed laser pulse. It is this synchronization, in combination with the fact that the generated ions are practically monoenergetic, which finally opens the door for time resolved experiments in the field of ion–surface interaction, particularly in the low (keV) energy range where such experiments have long been deemed impossible. Moreover, the observation that the achieved temporal pulse width is entirely determined by the thermal spread of the ionized gas atoms clearly demonstrates the potential to generate even shorter pulses via cooling of the neutral gas target such as done, for instance, in ion momentum recoil spectrometry reaction microscope experiments [34–38]. In fact, the discussion presented in reference [15] already suggests that the use of an ultracold molecular beam target such as used in the reaction microscope should lead to a significant shortening of the measured ion pulse duration. Our simulations suggest that our setup allows the generation of ultrashort Ar^{+} ion pulses at keV ion energies with a duration in the single picosecond regime using this concept, and we are currently working on the experimental realization of this expectation by combining the ion source investigated here with a supersonic neutral gas beam as described in reference [27]. The concept also allows the generation of other rare gas ions such as He^{q+}, Ne^{q+} or Xe^{q+} or any other ions which can be derived from a gas phase neutral atom target.

Acknowledgment

The authors are greatly indebted to Ping Zhou for his assistance with the laser system. We thank the Deutsche Forschungsgemeinschaft (DFG) for their financial support of project C05 within the Collaborative Research Center (CRC) 1242 'Non-equilibrium dynamics in the time domain' (Project number 278162697).

Author contributions

AW, MS and KS-T conceptualized, supervised and led the project, KS-T provided assistance regarding the laser system, AG and LD carried out the measurements with help from LB, AG analyzed the data with input from AW and LB, PK performed the simulation, AG wrote the manuscript with review and editing assistance by AW and MS.

Data availability statement

All data that support the findings of this study are included within the article (and any supplementary files).

Conflict of interest

There authors declare no competing interests.

ORCID iDs

Andreas Wucher https://orcid.org/0000-0002-9244-9491

References

[1] Li J, Stein D, McMullan C, Branton D, Aziz M J and Golovchenko J A 2001 Ion-beam sculpting at nanometre length scales *Nature* **412** 166–9
[2] Krasheninnikov A V and Banhart F 2007 Engineering of nanostructured carbon materials with electron or ion beams *Nat. Mater.* **6** 723–33
[3] Hayworth K J, Peale D, Januszewski M, Knott G W, Lu Z, Xu C S and Hess H F 2020 Gas cluster ion beam SEM for imaging of large tissue samples with 10 nm isotropic resolution *Nat. Methods* **17** 68–71
[4] Aramesh M, Mayamei Y, Wolff A and Ostrikov K K 2018 Superplastic nanoscale pore shaping by ion irradiation *Nat. Commun.* **9** 835
[5] Twedt K A, Zou J, Davanco M, Srinivasan K, McClelland J J and Aksyuk V A 2016 Imaging nanophotonic modes of microresonators using a focused ion beam *Nat. Photon.* **10** 35
[6] Saka S K, Vogts A, Kröhnert K, Hillion F, Rizzoli S O and Wessels J T 2014 Correlated optical and isotopic nanoscopy *Nat. Commun.* **5** 3664
[7] Zhou Y *et al* 2020 Real-time mass spectrometric characterization of the solid-electrolyte interphase of a lithium-ion battery *Nat. Nanotechnol.* **15** 224–30
[8] Gaebel T *et al* 2006 Room-temperature coherent coupling of single spins in diamond *Nat. Phys.* **2** 408–13
[9] Dolde F *et al* 2013 Room-temperature entanglement between single defect spins in diamond *Nat. Phys.* **9** 139–43
[10] Schröder T *et al* 2017 Scalable focused ion beam creation of nearly lifetime-limited single quantum emitters in diamond nanostructures *Nat. Commun.* **8** 15376
[11] Lühmann T, John R, Wunderlich R, Meijer J and Pezzagna S 2019 Coulomb-driven single defect engineering for scalable qubits and spin sensors in diamond *Nat. Commun.* **10** 4956
[12] Hellborg R, Whitlow H J and Zhang Y 2009 *Ion Beams in Nanoscience and Technology* (Berlin: Springer)
[13] Chini M, Zhao K and Chang Z 2014 The generation, characterization and applications of broadband isolated attosecond pulses *Nat. Photon.* **8** 178
[14] Gaumnitz T, Jain A, Pertot Y, Huppert M, Jordan I, Ardana-Lamas F and Wörner H J 2017 Streaking of 43-attosecond soft-x-ray pulses generated by a passively CEP-stable mid-infrared driver *Opt. Express* **25** 27506–18
[15] Höhr C, Fischer D, Moshammer R, Dorn A and Ullrich J 2008 A subnanosecond pulsed ion source for micrometer focused ion beams *Rev. Sci. Instrum.* **79** 053102
[16] Harrison D E Jr 1988 Application of molecular dynamics simulations to the study of ion-bombarded metal surfaces *Crit. Rev. Solid State Mater. Sci.* **14** 1–78
[17] Urbassek H 2006 *Sputter theory.* Ion-beam science–solved and unsolved problems *Mat.-Fys. Medd. K. Dan. Vidensk. Selsk.* **52** 433–63
[18] Garrison B J and Postawa Z 2008 Computational view of surface based organic mass spectrometry *Mass Spectrom. Rev.* **27** 289–315
[19] Weidtmann B, Duvenbeck A and Wucher A 2008 Predicting secondary ion formation in molecular dynamics simulations of sputtering *Appl. Surf. Sci.* **255** 813–5
[20] Lehtinen O, Kotakoski J, Krasheninnikov A, Tolvanen A, Nordlund K and Keinonen J 2010 Effects of ion bombardment on a two-dimensional target: atomistic simulations of graphene irradiation *Phys. Rev.* B **81** 153401
[21] Duvenbeck A, Weidtmann B and Wucher A 2010 Predicting kinetic electron emission in molecular dynamics simulations of sputtering *J. Phys. Chem.* C **114** 5715–20
[22] Wucher A and Duvenbeck A 2011 Kinetic excitation of metallic solids: progress towards a microscopic model *Nucl. Instrum. Methods Phys. Res.* B **269** 1655–60
[23] Darkins R and Duffy D M 2018 Modelling radiation effects in solids with two-temperature molecular dynamics *Comput. Mater. Sci.* **147** 145–53
[24] Aumayr F *et al* 2019 Roadmap on photonic, electronic and atomic collision physics: III. Heavy particles: with zero to relativistic speeds *J. Phys. B: At. Mol. Opt. Phys.* **52** 171003
[25] Kollmer F 2004 Cluster primary ion bombardment of organic materials *Appl. Surf. Sci.* **231–232** 153–8
[26] Linnarsson M K, Hallén A, Åström J, Primetzhofer D, Legendre S and Possnert G 2012 New beam line for time-of-flight medium energy ion scattering with large area position sensitive detector *Rev. Sci. Instrum.* **83** 095107
[27] Breuers A, Herder M, Kucharczyk P, Schleberger M, Sokolowski-Tinten K and Wucher A 2019 A concept to generate ultrashort ion pulses for pump–probe experiments in the keV energy range *New J. Phys.* **21** 053017
[28] Wiley W C and McLaren I H 1955 Time-of-flight mass spectrometer with improved resolution *Rev. Sci. Instrum.* **26** 1150–7
[29] Augst S, Strickland D, Meyerhofer D D, Chin S-L and Eberly J H 1989 Tunneling ionization of noble gases in a high-intensity laser field *Phys. Rev. Lett.* **63** 2212–5
[30] Kucharczyk P, Golombek A and Wucher A 2020 Generation of ultrashort ion pulses in the keV range: numerical simulations *Nucl. Instrum. Methods Phys. Res.* B **483** 41–9
[31] Augst S, Meyerhofer D D, Strickland D and Chint S L 1991 Laser ionization of noble gases by Coulomb-barrier suppression *J. Opt. Soc. Am.* B **8** 858–67
[32] Hansch P, Walker M and Van Woerkom L 1996 Spatially dependent multiphoton multiple ionization *Phys. Rev.* A **54** 2559–62
[33] Ammosov M V, Delone N B and Krainov V B 1986 Tunnel ionization of complex atoms and atomic ions in alternating electromagnetic fields *Soviet Physics - JETP* **64** 1191–4
[34] Liu Y *et al* 2010 Multiphoton double ionization of Ar and Ne close to threshold *Phys. Rev. Lett.* **104** 173002
[35] Zrost K, Rudenko A, Ergler T, Feuerstein B, Jesus V L B d, Schröter C D, Moshammer R and Ullrich J 2006 Multiple ionization of Ne and Ar by intense 25 fs laser pulses: few-electron dynamics studied with ion momentum spectroscopy *J. Phys. B: At. Mol. Opt. Phys.* **39** S371

[36] Feuerstein B et al 2001 Separation of recollision mechanisms in nonsequential strong field double ionization of Ar: the role of excitation tunneling Phys. Rev. Lett. 87 043003
[37] Moshammer R et al 2000 Momentum distributions of Ne^{n+} Ions created by an intense ultrashort laser pulse Phys. Rev. Lett. 84 447
[38] Ullrich J, Moshammer R, Dörner R, Jagutzki O, Mergel V, Schmidt-Böcking H and Spielberger L 1997 Recoil-ion momentum spectroscopy J. Phys. B: At. Mol. Opt. Phys. 30 2917